

Principal bed states during SandyDuck97: Occurrence, spectral anisotropy, and the bed state storm cycle

Alex E. Hay and Todd Mudge

Department of Oceanography, Dalhousie University, Halifax, Nova Scotia, Canada

Received 25 April 2004; revised 16 August 2004; accepted 8 December 2004; published 12 March 2005.

[1] Results are presented from 70+ days of nearly continuous in situ acoustic imagery of the nearshore sandy seabed in ~ 3 -m mean water depth, at two locations separated by 40-m cross-shore distance. The bottom sediments were 150 μm median diameter sand, with nearly identical size distributions at the two locations. Five principal bed states were observed: irregular ripples, cross ripples, linear transition ripples, lunate megaripples, and flat bed. The linear transition and flat bed states were the most frequent, together accounting for 68% of the total time. Bed state occurrence was a strong function of incident wave energy, each bed state occurring within a relatively narrow range of sea-and-swell energies. During the 12 major storm events spanned by the record, the bed response was characterized by a repeatable bed state storm cycle, involving four of the five principal states (lunate megaripples did not appear repeatedly, and thus may be a special case), with no obvious dependence of bed state occurrence on prior bed state, or on third-moment measures of wave nonlinearity. Radial spectra from the rotary acoustic images indicate pronounced differences in the anisotropy of spatial scales for the different bed states, and exhibit onshore-offshore differences which are likely related to ripple migration.

Citation: Hay, A. E., and T. Mudge (2005), Principal bed states during SandyDuck97: Occurrence, spectral anisotropy, and the bed state storm cycle, *J. Geophys. Res.*, 110, C03013, doi:10.1029/2004JC002451.

1. Introduction

[2] Clifton [1976] proposed a conceptual model of bed-form development in nearshore sandy environments which, in addition to sediment grain size and the incident wave period, depends upon the wave orbital velocity amplitude and the velocity amplitude difference between the shoreward and seaward strokes of individual incident waves. Clifton based his model on field observations of a shoreward progression of bed states, inferring that this progression was at least partly governed by shoreward changes in the properties of the wave forcing. These hard-won observations [see Clifton *et al.*, 1971] were obtained using SCUBA during nonstorm conditions, and with limited simultaneous measurements of the hydrodynamic forcing.

[3] An analogous succession of nearshore bed states has been identified in more recent observations of sand bed response at fixed locations during storm events [Hay and Wilson, 1994; Smyth *et al.*, 2002]. The striking similarities between the spatial progression of bed states across the beach face during nonstorm conditions and the temporal progression locally during storms support the central idea underlying Clifton's model: that nearshore bed state is closely related to the statistical properties of the wave forcing. The question is, which of the wave parameters

suggested by Clifton, wave amplitude or amplitude difference, is the more important?

[4] The bed state observations reported by Hay and Wilson [1994] and Smyth *et al.* [2002] are each limited by the short duration of the respective time series. These data sets therefore do not provide an adequate number of realizations for testing the predictions of Clifton's [1976] model. In this paper, results are presented from a much more extensive set of observations acquired during the 1997 SandyDuck experiment. Over the 10-week duration of the experiment, the bed response to more than a dozen storm events was captured at multiple cross-shore locations. Here we focus on data from two of those locations for which the grain size was nearly the same and the data sets were the most complete. Our primary purpose is to determine whether bed state is related mainly to second-order (e.g., energy) or third-order (e.g., skewness or asymmetry) statistics of the incident wave field.

[5] The paper is organized as follows. The experimental and analysis methods are outlined in the section 2. The results are presented in section 3, beginning with an intercomparison of second- and third-moment statistics obtained from the different velocimeters and surface elevation detectors (pressure sensors and upward looking sonars) across the instrument array. Observed second-order velocity moments are also compared to those predicted from pressure and surface elevation variance by linear surface gravity wave theory. The purpose of these intercomparisons is to demonstrate that the observed wave orbital velocity moments are self-consistent

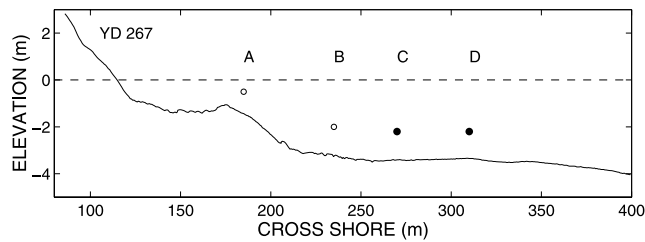


Figure 1. Bathymetry on yearday 267 (24 September), 1997, showing locations of instrument frames. The rotary fan beam sonar imagery discussed here was acquired at Frames C and D (solid dots). Cross-shore distances are in FRF coordinates.

in the sense that: (1) different sensors yield comparable values and (2) the second-order statistics of measurements at depth are consistent with linear wave theory [Guza and Thornton, 1980]. The remainder of section 3 focuses on the observed bed states: the occurrence of different bed states relative to the hydrodynamic forcing statistics (section 3.4), ensemble-averaged bed state spectra and their variation with azimuth (i.e., anisotropy) (section 3.5), the dominant spatial scales (section 3.6), and the bed state storm cycle (section 3.7). The results are compared to Clifton's conceptual model in section 4, which is followed by the summary and concluding remarks in section 5.

2. Methods

2.1. Field Experiment

[6] SandyDuck97 (SD97) was carried out at the U.S. Army Corps of Engineers Field Research Facility (FRF) in Duck, North Carolina. The FRF is described by Birkemeier *et al.* [1985]. The data presented here are from a cross-shore instrument array deployed at the north end of the FRF property, as far away from the FRF pier as possible (500 m to the north). The instrument frame locations are indicated in Figure 1.

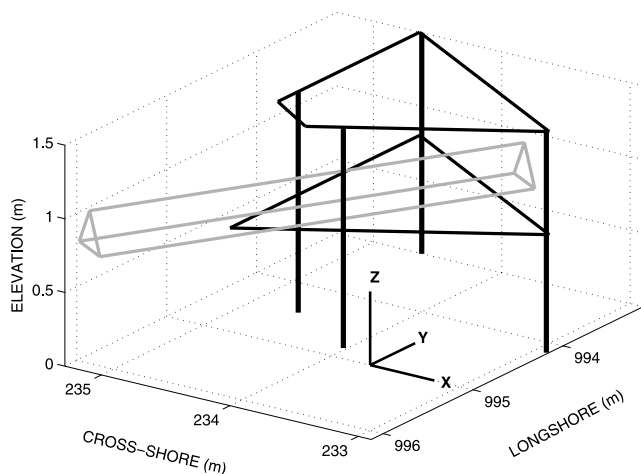


Figure 2. Sketch of the instrument frame, to scale, showing instrument mast (shaded) and the space frame and four vertical support pipes (black). Longshore and cross-shore distances are in FRF coordinates, and the xyz coordinate system also shown.

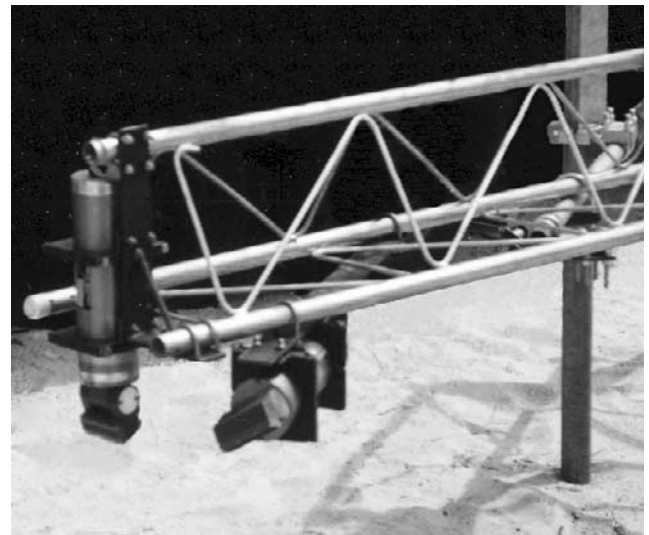


Figure 3. Photograph of rotary sonars mounted on the mast. The fanbeam sonar is at the extreme left, with pressure case mounted vertically. The pencil beam was mounted slightly to the right, with its pressure case horizontal, as shown (a second fanbeam unit is actually shown). The northeast frame post is visible at the extreme right. The EM flowmeter and pressure sensor port were mounted on a 1.2-cm-diameter vertical rod attached to the mast. The sonar pressure cases (30 cm long by 9 cm diameter) provide a scale.

[7] The instrument frame design is sketched in Figure 2. The sensors were mounted at the outboard end of a cantilever arm at a nominal height of 1 m above bottom (Figure 3). The cantilever design allowed the instruments to be deployed away from the frame and its support legs, thus minimizing frame-induced disturbance of the bed in the immediate vicinity of the instruments, and reducing obstruction by frame elements of the fanbeam sonar field of view. The cantilever was a 10-foot long antenna mast section manufactured from 3.2-cm-diameter galvanized steel tubing and 0.8-cm-diameter rod webbing (see Figure 3). The frames were constructed from 3.4-cm-diameter steel pipe. The legs were 6-m-long, 6.1-cm-diameter Schedule 80 galvanized steel pipes, jettied vertically into the sand to a depth of about 4.5 m below the sediment-water interface. The mast section was oriented toward the northeast, at an angle of about 60° (Table 1) to the instrument line, in order to project the instruments into the strong southward flowing longshore currents produced during nor'easters (storms with typically gale-

Table 1. Frame Locations, Orientation Angles, Mean Water Depth h , and Grain Size^a

| Frame | Cross Shore, m | Longshore, m | Angle, deg | h , m | d_{16} , μm | d_{50} , μm | d_{84} , μm |
|-------|----------------|--------------|------------|---------|--------------------------|--------------------------|--------------------------|
| C | 270 | 995 | 58 | 3.36 | 117 | 145 | 195 |
| D | 310 | 995 | 61 | 3.29 | 119 | 148 | 195 |

^aGrain size: median diameter d_{50} , and d_{16} and d_{84} , the subscripts denoting cumulative percent finer. Grain sizes are the means of three samples collected at different times over the course of the experiment. Frame locations are in FRF coordinates.

force northeasterly winds which occur in the Outer Banks area in the autumn).

2.2. Instrumentation

[8] Viatran pressure sensors and Marsh-McBirney electromagnetic (EM) flowmeters were mounted on each instrument frame, the EM at a nominal height above bottom of 35 cm. This height, of course, changed as the local bed elevation evolved, and the vertical positions of the EMs and pressure sensor ports were adjusted from time to time by SCUBA divers to compensate. A 5-MHz acoustic Doppler velocimeter (Sontek ADV-O) was mounted on Frame B at 2.46 m depth below NGVD (National Geodetic Vertical Datum), with its sampling volume at 56 cm mean height above bottom. The ADV-O was sampled at 25 Hz for about 23.5 min, every 0.5 hours. The EM flowmeters and pressure sensors were sampled at 2 Hz continuously, with records stored at 0.5-hour intervals. (See work by *Henderson and Bowen* [2002] for further discussion and analysis of the EM and pressure sensor data.) Water temperature was sampled at 2 Hz and 1-min averages stored.

[9] The seabed was imaged using Kongsberg Simrad Mesotech Model 971 rotary fanbeam sonars (Figure 3). These sonars [*Hay and Wilson*, 1994] operate at 2.25 MHz and have rectangular transducers with beam patterns 30° wide in the vertical, and 0.8° wide in the horizontal (beamwidths are between -3 dB points). Transducer depths were 2.65 m (Frame C) and 2.53 m (Frame D) or, using the mean water depths listed in Table 1, at 71-cm and 76-cm mean heights above bottom, respectively. The transducer assembly is driven in azimuth via a stepper motor in 0.225° increments. The data acquisition system was configured to acquire five complete images with 0.45° resolution in azimuth, and 9-mm resolution in range. The transmit pulse duration was 10 μ s. The backscatter signal was digitized (12-bit resolution) at 250 kHz, and three-point block averaged. The units transmitted at each 0.225° step, and the backscatter profiles from two consecutive steps were averaged together. The block averaging in range and profile averaging in azimuth were implemented to reduce speckle noise in the individual 9.5-m-diameter images. Each set of five images was acquired in about 3.7 min (≈ 40 s per 360° image), at 10-min intervals during storm events and at 30-min intervals during the periods of relative calm between storms. This judgment was based on current wave conditions and the weather forecast.

2.3. Sonar Image Processing

[10] The five images in each set were combined to produce a single composite image. This was done to reduce the effects of intermittent noise arising during SD97 mainly from (1) masking of the seabed returns by sediment suspension events and/or bubble clouds injected by breaking waves and (2) shadows cast on the seabed by fish swimming through the acoustic beam. The former was important only during storm conditions; the latter was important only during the relatively inactive periods between storms. Breaking and suspension events are intermittent and three-dimensional and occur on wave period timescales. Bubble and suspension clouds therefore

tend to degrade only portions of each 360-degree image, since several waves go by during the 40-s image acquisition interval. Similarly, fish shadows affect only part of the image, and are fleeting compared to the image acquisition time. All of these noise sources reduce the backscatter amplitude from the seabed. We therefore ranked the profiles at each azimuth by total “brightness” (i.e., backscatter amplitude integrated with respect to range). The final image was constructed from the average of the four brightest profiles at each azimuth. The total number of composite fanbeam images was 6820 at frame C, and 6774 at frame D.

[11] The range-azimuth backscatter profiles were slant-range corrected and linearly interpolated to x - y Cartesian coordinates at 0.9×0.9 cm resolution. An effective transducer beam pattern for each fanbeam sonar was obtained by averaging many images together, after first correcting for gain changes made in the shore-based signal conditioning electronics and for the time-variable gain in the instrument. This beam pattern represents the effective gain as a function of angle from the vertical. The backscatter profiles were corrected by dividing by this angle-dependent gain factor, taking the sonar height above bottom and local on-offshore bottom slope into account.

2.4. Bed State Determination

[12] Bed state was determined by human operators manually scanning through the fanbeam imagery. With an image displayed on the computer screen, the operator entered a code into a database indicating to which of a predetermined set of bed state types the image best conformed. If more than one ripple type was present in the sonar image, the operator would include the code corresponding to each type in the database entry for that image. Three different operators went through the imagery. When results among operators differed, the image in question was discussed and a category agreed upon. In most cases these differences occurred during the periods of transition from one bed state to another, and especially for transitions between irregular ripples and cross ripples.

2.5. Forcing Statistics

[13] Velocity and pressure statistics were estimated from the 1/2-hour duration data runs. The time series were partitioned into (1) record mean U , V , and P ; (2) sea-and-swell band u_w , v_w , and p_w constituents (0.05–0.3 Hz); and (3) infragravity band u_{IG} , v_{IG} , and p_{IG} constituents (<0.05 Hz). The sea-and-swell and infragravity band constituents were obtained using forward and reverse passes of a fifth-order Butterworth digital filter. The rms wave orbital velocity in the sea-and-swell band is defined as

$$u_{rms} = \langle u_w^2 + v_w^2 \rangle^{1/2}, \quad (1)$$

and the significant wave orbital velocity is defined as $u_{1/3} = 2u_{rms}$ [*Thornton and Guza*, 1983]. The rms infragravity wave velocity is defined similarly: $U_{rms}^{IG} = \langle u_{IG}^2 + v_{IG}^2 \rangle^{1/2}$. The u -components are positive shoreward, and the v -components are positive toward the south (i.e., the directions of positive x and y , Figure 2).

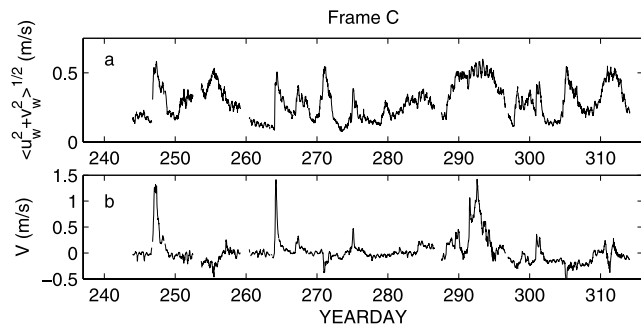


Figure 4. Time series of (a) rms wave orbital velocity and (b) longshore current V . Frame C.

[14] Skewness, Sk , and asymmetry, As , were computed from the sea-and-swell band velocity and pressure signals as follows:

$$Sk(x) = \langle x^3 \rangle / \langle x^2 \rangle^{3/2} \quad (2)$$

$$As(x) = Sk[\Im\{\mathcal{H}(x)\}], \quad (3)$$

where $\mathcal{H}(x)$ is the Hilbert transform of x , and \Im denotes the imaginary part. Note that this definition of asymmetry gives values identical in magnitude but opposite in sign to those reported by *Elgar et al.* [1990] [see also *Elgar*, 1987].

[15] The incident wave direction, α , in the sea-and-swell band was determined from [*Fofonoff*, 1969]

$$\tan 2\alpha = \frac{2\langle u_w v_w \rangle}{u_w^2 - v_w^2}. \quad (4)$$

2.6. Spectral Analysis

[16] Velocity and pressure spectra were estimated from the 1/2-hour long records using Hanning-windowed, linearly detrended 200-point data segments with 50% overlap. The resulting spectra had 0.1-Hz resolution, and 66 equivalent degrees of freedom. The peak wave period, T_p , corresponds to the peak in the u spectrum.

[17] Backscatter spectra as a function of radial wave-number were determined from the fanbeam backscatter profiles. The segment length was 1.8 m. A Hanning window and 50% overlap between segments were applied. The resulting spectra had 0.56 cycle/m resolution. Spectra from 10 adjacent profiles were averaged together, yielding ensemble-averaged spectra at 4.5° intervals in azimuth with 58 equivalent degrees of freedom.

3. Results

3.1. Forcing Time Series

[18] Time series of rms wave orbital velocity and longshore current at Frame C are shown in Figure 4 for the duration of SandyDuck97. There are some gaps in the velocity measurements; these are due either to periods when the instrumentation was turned off for routine maintenance or cleaning by SCUBA divers, or to data acquisition system maintenance. As indicated by the periods of high incident

wave energy, approximately 12 separate storm events occurred during the 70-day length of the record.

3.2. Wave Energy, Skewness, and Asymmetry

[19] As stated in section 1, the primary purpose of this study is to determine whether bed state during SD97 was related mainly to the second-order (e.g., energy) or third-order (e.g., skewness or asymmetry) statistics of the incident wave field. In order to make this determination, it is necessary first to demonstrate that our estimates of the second- and third-order moments are reliable. We do so in this section by showing that (1) the observed wave orbital velocity moments from different sensors are in agreement, (2) the second-order statistics of measurements at depth are consistent with linear wave theory, and (3) our estimates of skewness and asymmetry are comparable to those obtained by other SD97 investigators at similar cross-shore locations.

[20] The second- and third-order moments of the sea-and-swell band forcing, as registered by the EM flowmeters and pressure sensors at frames C and D, are presented in Figure 5. In addition to summarizing the ranges of these forcing parameters, the figure represents a test of the consistency of the second-moment measurements with linear wave theory, and a test of the consistency of the third-moment estimates among the different sensors and between instrument frames.

[21] Pressure variance is plotted against velocity variance in Figures 5a and 5b. Pressure variance is scaled by g/h to give the equivalent velocity variance assuming linear shallow water wave theory [e.g., *Kundu*, 1990]. At frame C, the pressure and velocity variances are for the most part consistent with the g/h scaling. The data from frame D similarly cluster about the 1:1 line. Thus the agreement between the measured velocity variance and g/h -scaled pressure variance is on the whole satisfactory ($R^2 \geq 0.93$). As a further check, we have also made comparisons between the sea surface elevation variance measured with upward looking sonars and the measured pressure variance, across the full width of the array. These results (see Appendix A, Figure A1) demonstrate quite good agreement between the pressure variance and sea surface elevation variance.

[22] The pressure skewness, Sk_p , and velocity skewness, Sk_u (u -component only), are plotted in Figures 5c and 5d. The points for both frames cluster nicely about a line parallel to the 1:1 line, but displaced slightly below. The tendency toward lower values of Sk_p is likely due to the slower frequency response of the pressure sensor relative to the EM flowmeter. This suggestion is supported by the comparisons between Sk_p and the surface elevation skewness, Sk_η , determined from the upward looking sonar data (see Appendix A, Figure A2), which exhibit similar offsets to low Sk_p . Note the range of Sk_u values, from about -0.1 to 1.5 , and that the values are mostly positive, indicating peakier crests and broader troughs on average.

[23] Pressure and velocity asymmetry, As_p and As_u , are shown in Figures 5e and 5f. While the scatter among the points is greater than for skewness, the values for the two sensor types are in broad agreement for both frames. The points range from -0.6 to $+0.2$, with a tendency for the values at frame C to be more positive.

[24] As a final comparison, an acoustic Doppler velocimeter (ADV) was deployed at frame B in addition to the EM

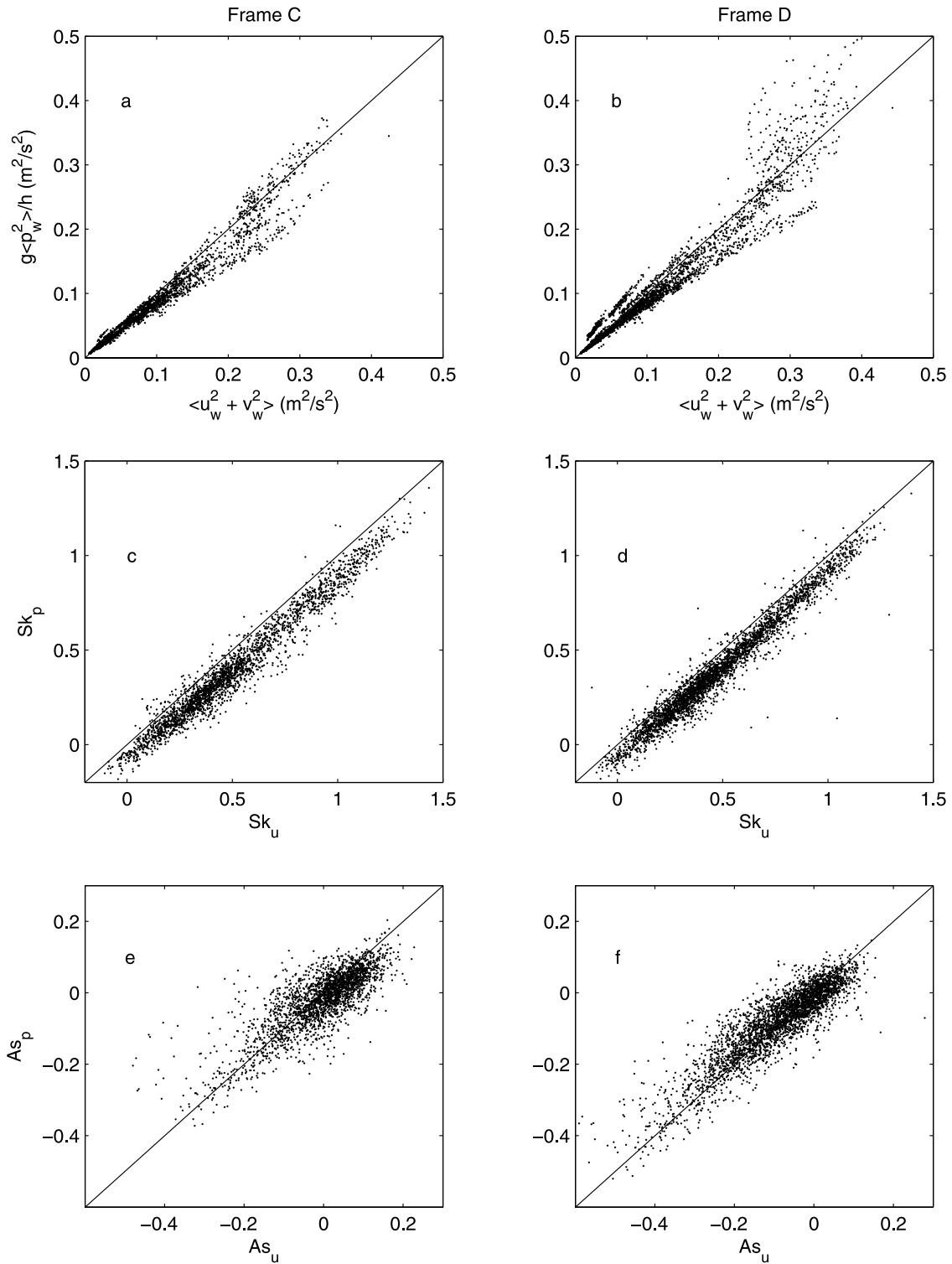


Figure 5. Comparisons between second and third moments of the pressure and velocity sensor records in the sea-and-swell band (0.05 to 0.3 Hz) at frames (left) C and (right) D for (a, b) pressure variance, converted to velocity variance assuming shallow water linear wave theory, versus EM flowmeter velocity variance $\langle u_w^2 + v_w^2 \rangle$; (c, d) pressure skewness Sk_p versus EM flowmeter velocity skewness Sk_u ; (e, f) pressure asymmetry As_p versus EM flowmeter velocity asymmetry As_u . Solid lines indicate 1:1 relationship. Values of $R^2 \pm 95\%$ confidence intervals are as follows: Figure 5a, 0.96 ± 0.003 ; Figure 5b, 0.93 ± 0.004 ; Figure 5c, 0.96 ± 0.003 ; Figure 5d, 0.62 ± 0.02 ; Figure 5e, 0.64 ± 0.02 ; and Figure 5f, 0.81 ± 0.01 .

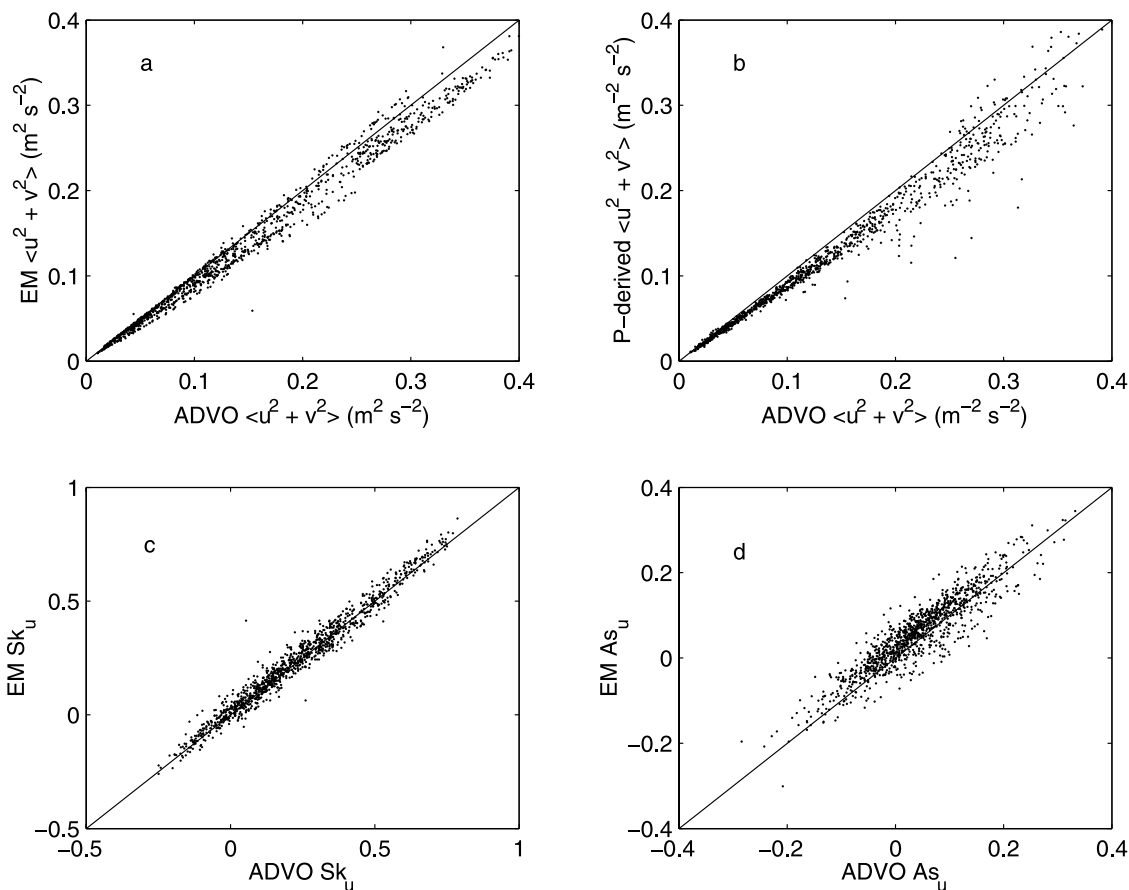


Figure 6. Comparisons of second and third moments in the sea-and-swell band similar to those in Figure 5, but at Frame B and including comparisons between an EM flowmeter and an acoustic Doppler velocimeter (ADV-O): (a) sea-and-swell variance $\langle u^2 + v^2 \rangle$, EM versus ADV-O; (b) pressure variance, converted to velocity variance assuming linear wave theory, and the ADV-O velocity variance; (c) skewness Sk_u , EM versus ADV-O; and (d) asymmetry As_u , EM versus ADV-O. R^2 values are as follows: Figure 6a, 0.987; Figure 6b, 0.970; Figure 6c, 0.947; and Figure 6d, 0.843. Best-fit slopes $m \pm 95\%$ bootstrap confidence intervals are as follows: Figure 6a, 0.937 ± 0.002 ; Figure 6b, 0.909 ± 0.005 ; Figure 6c, 0.988 ± 0.005 ; and Figure 6d, 0.90 ± 0.013 .

flowmeter, and the records from this additional sensor provide another consistency check on the velocity moment data. Comparisons of the ADV velocity variance to that from the EM flowmeter, and to the velocity-scaled pressure variance, are shown in Figures 6a and 6b. The overall agreement is again quite good. The EM and ADV skewness values are in excellent agreement; in particular, the obvious offset in the Sk_p and EM Sk_u comparisons is not evident. The asymmetries are also in good agreement, and the ADV results again confirm the frequent occurrence of positive asymmetry.

[25] In our sign convention, positive asymmetry indicates waves which are pitched seaward. The usual expectation in the nearshore zone is that prior to breaking, waves become increasingly pitched shoreward as they shoal, as observed by *Elgar et al.* [1990] in nearshore environments on the U.S. Pacific coast, for example. Thus the large number of our data runs with positive asymmetry was somewhat surprising, and prompted comparisons with the sea surface elevation asymmetries As_η obtained from the upward looking sonar data as a further check. These comparisons (see Appendix A, Figure A2) yield the same result; that is, the As_η values were also frequently positive at frames B, C, and

D. Predominantly pitched-shoreward waves occurred only at frame A, the location nearest the shoreline. Thus there is agreement among 10 different sensors of four different types on three different frames, and hence compelling evidence for the frequent occurrence of pitched-seaward asymmetry at intermediate distances from the shoreline during SD97.

[26] Using data from additional instruments deployed during SD97 to the south of our frame locations, *Herbers et al.* [2003] also obtained pitched-seaward asymmetries at cross-shore distances comparable to frames B, C, and D (i.e., between 200 and 300 m in FRF coordinates). The waves were pitched dominantly shoreward only inside 200 m (as at frame A), or beyond 300 m. While *Herbers et al.* [2003] present results for only 1 day (10 August), the observed values of asymmetry are well reproduced by their nonlinear wave shoaling model (see their Figure 3 and related text). Thus a likely physical explanation for the pitched-seaward asymmetries at intermediate distances from the shoreline is a reversal in the sign of energy transfer from the fundamental to the harmonics in the area between the two bars.

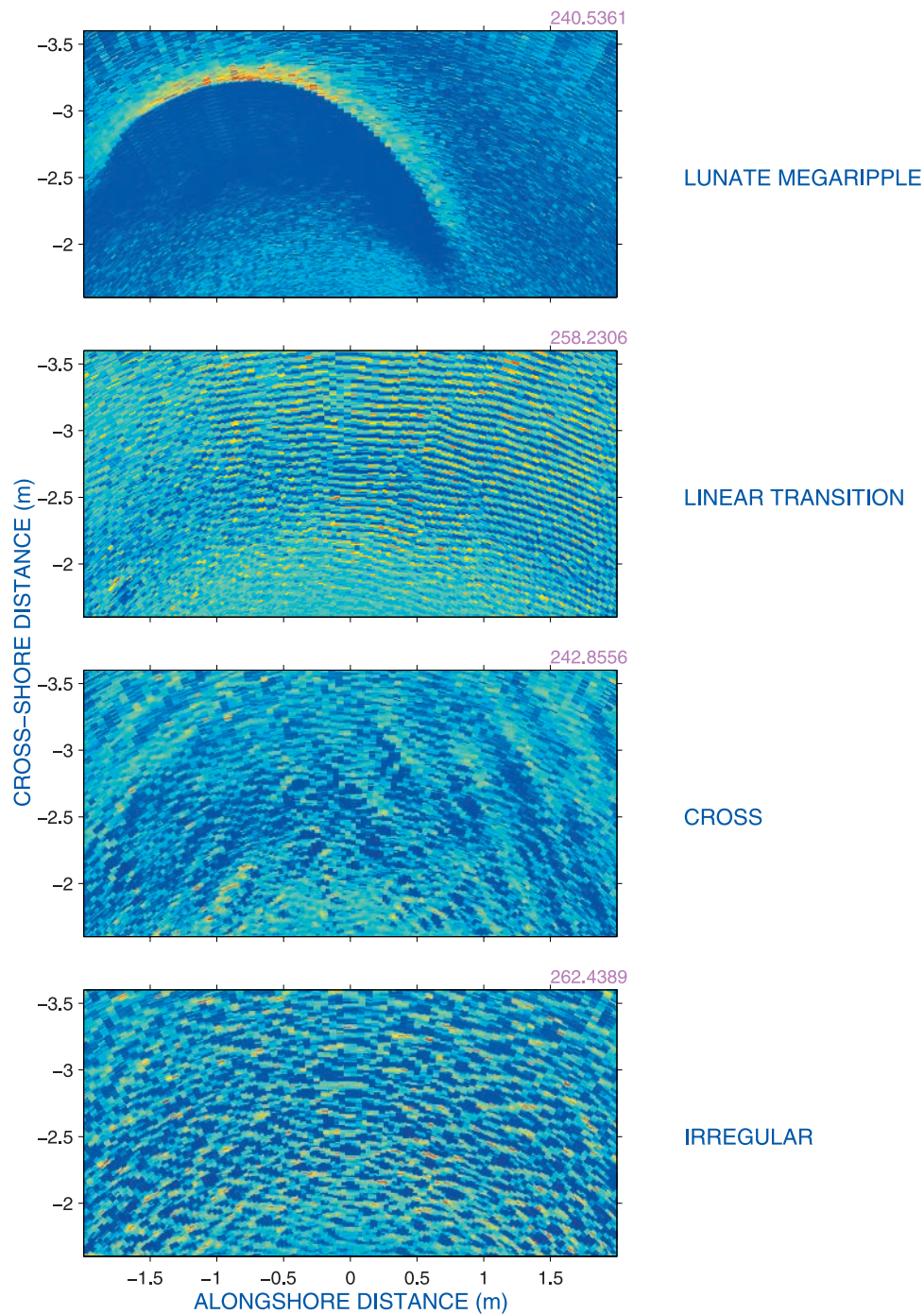


Figure 7. The $2\text{-m} \times 4\text{-m}$ subarea acoustic images of the seabed taken from the 9.5-m diameter fanbeam images, showing four of the five principal bed states: (top to bottom) a lunate megaripple, linear transition ripples, cross ripples, and irregular ripples. The fifth principal bed state was flat bed for which the fan beam images are featureless, and is not shown. The subimages are from the offshore side of Frame C. Color scale indicates backscatter amplitude, with blue low and red high. Cross-shore (x) and alongshore (y) distances are centered at the fanbeam axis of rotation, with the sign convention indicated in Figure 2; that is, increasing negative values of the cross-shore coordinate indicate the offshore direction.

3.3. Bed State Images

[27] Figure 7 shows $2\text{-m} \times 4\text{-m}$ subsections of the 9.5-m -diameter fanbeam images. These subimages illustrate the qualitative appearance of the different bed states discussed here: from top to bottom, a shoreward facing lunate mega-

ripple; linear transition ripples; cross ripples; and irregular ripples. The color scale in the images is proportional to backscatter amplitude, with blue corresponding to low amplitudes and red to high. Flat bed is not shown, but a similar subimage for the flat bed case has been presented by

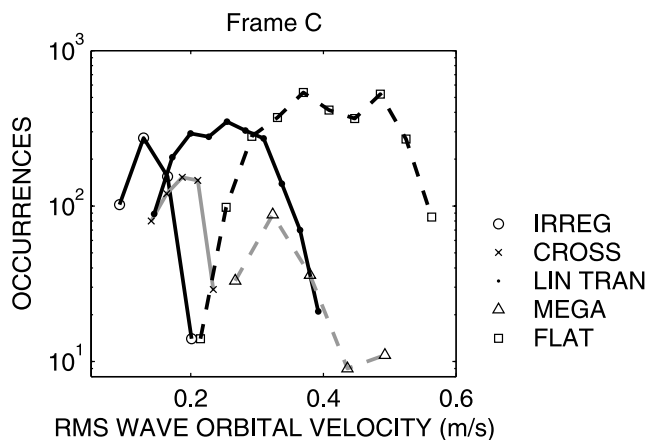


Figure 8. Bed state occurrence versus rms wave orbital velocity $\langle u^2 + v^2 \rangle^{1/2}$ at frame C. Different bed states, indicated by symbols and line types, are as follows: irregular ripples (circles, solid black line); cross ripples (crosses, solid shaded line); linear transition ripples (dots, solid black line); lunate megaripples (triangles, dashed shaded line); and flat bed (squares, dashed black line).

Smyth et al. [2002], together with representative subimages for the other bed states (except lunate megaripples) for comparison to those in Figure 7. The subimages of *Smyth et al.* [2002] are also for fine sand (174 μm median diameter), but from the 1995 Queensland Beach nearshore experiment (QB95).

[28] Lunate megaripples are characterized by deep, crescentic troughs [*Clifton et al.*, 1971]: The megaripple trough in Figure 7 (top panel) is the broad crescentic acoustic shadow region bounded on its seaward side by the high-amplitude reflection from the shoreward facing slope. Similar planform acoustic images of shoreward facing lunate megaripples have been reported elsewhere [*Hay and Wilson*, 1994; *Ngusaru and Hay*, 2004]. Bed elevation profiles across these features have been obtained either by monitoring bed elevation as a function of time as megaripples migrated past fixed sonar altimeters [*Hay and Bowen*, 1993; *Gallagher et al.*, 1998], or instantaneously using rotary pencil-beam sonars [*Ngusaru and Hay*, 2004].

[29] Linear transition ripples are low-relief, short-wavelength ripples occurring at wave energies just below the transition to flat bed [*Dingler and Inman*, 1977; *Conley and Inman*, 1992; *Crawford and Hay*, 2001]. In the ripple classification scheme proposed by *Clifton and Dingler* [1984], linear transition ripples are of the anorbital type, that is, with wavelengths much less than the nearbed wave orbital diameter [*Crawford and Hay*, 2001]. As indicated by the subimage in Figure 7, these ripples also tend to be very long-crested. High-resolution bed elevation profiles of linear transition ripples have been reported by *Dingler and Inman* [1977] and *Crawford and Hay* [2001].

[30] Cross ripples are characterized by short- and long-wavelength ripple components with crests inclined at relatively large angles ($\approx 20^\circ$) away from shore-parallel [*Hay and Wilson*, 1994]. As indicated in Figure 7, the longer wavelength component tends to be relatively long-crested, while the shorter wavelength component tends to be shorter-crested and to occupy the longer wavelength troughs.

[31] The “irregular” ripple type (bottom panel, Figure 7) is a category that we have adopted for sonar image classification. The irregular appearance of the bedforms in the images is due to short-crestedness and/or frequent bifurcations. The irregular ripple category likely encompasses several ripple types including the vortex or orbital ripple state since, as will be seen, the irregular bed state occurs at wave energies for which orbital and suborbital ripples would be expected to form. However, unlike the long-crested orbital ripples in medium-grained sand observed on the inner continental shelf [*Traykovski et al.*, 1999], we have yet to capture long-crested vortex ripples in our acoustic seabed imagery from nearshore environments with fine sand sediments (i.e., 200- μm median diameter). It is also possible that the irregular ripple category includes highly three-dimensional low-energy bedform types (e.g., brick-pattern ripples [*Sleath*, 1984]). The resolution of the acoustic images is not high enough to reveal such structure.

3.4. Bed State Occurrence

[32] Having demonstrated previously that measurements of second- and third-order moments of the wave forcing are self-consistent, we now seek relationships between the occurrence of different bed states and rms sea-and-swell wave orbital velocity, skewness and asymmetry. Figures 8 and 9 show the observed occurrences of the five bed states as a function of rms wave orbital velocity at frames C and D. The distributions are quite similar for the two locations: Irregular ripples occur at low values of u_{rms} , flat bed at high values, and linear transition ripples at intermediate values. The cross-ripple and megaripple states, respectively, occurred at frame C in the u_{rms} overlap regions between irregular and linear transition ripples, and between linear transition ripples and flat bed. At frame D, cross ripples also occurred in the overlap region between irregular and linear transition ripples. Lunate megaripples, however, occurred over a broader range of u_{rms} at frame D, but did not occur more frequently at D than at C, despite the indications in Figures 8 and 9 (see Table 3 in section 3.4 and Figure 14a in section 3.7).

[33] Figure 10 shows the dependence of bed state on velocity skewness, Sk_u , and asymmetry, As_u , at frame C. The Frame D data (not shown) are similar. For each of the

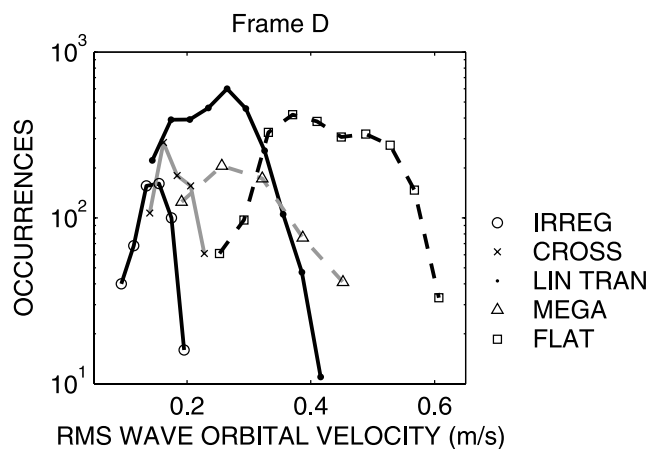


Figure 9. Bed state occurrence versus rms wave orbital velocity as in Figure 8, but for frame D.

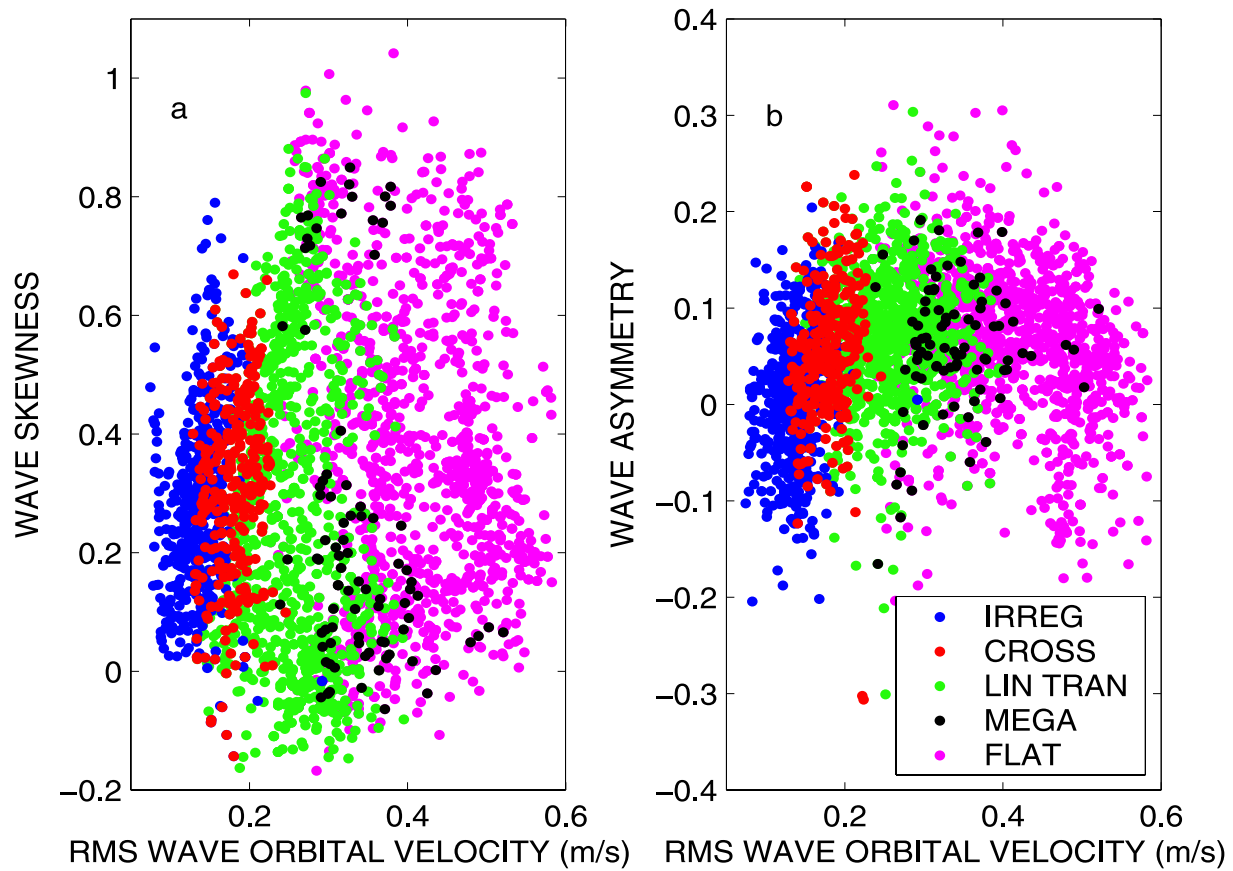


Figure 10. Bed state occurrence as a function of rms wave orbital velocity and (a) wave skewness and (b) wave asymmetry. Bed states are indicated by colored dots: irregular ripples (blue), cross ripples (red), linear transition ripples (green), lunate megaripples (black), and flat bed (magenta).

five bed states, and for each of Sk_u and As_u , the points fall within distinct vertical bands. Along the horizontal axis, these bands span u_{rms} values consistent with the distributions in Figure 8. In contrast, along the vertical axis the points are widely spread and span both positive and negative values, indicating little relationship between the occurrence of a particular bed state and the ordinate: little relationship, that is, with either wave orbital velocity skewness or asymmetry.

[34] Figure 11 is a similar scatter diagram of the dependence of bed state on longshore current. Again, the points are grouped with respect to u_{rms} . Again, there is little indication of bed state depending on the value of the ordinate. Flat bed, for example, occurs for both weak and strong longshore currents. Linear transition ripples and lunate megaripples also occurred for both weak and “moderate” longshore currents, as did irregular ripples and cross ripples.

[35] The overall means and standard deviations of the forcing parameters associated with the different bed states at the two frame locations are presented in Table 2. All of these parameters have been previously introduced except the grain roughness Shields parameter which is given by [e.g., Sleath, 1984]

$$\theta_{2.5} = \frac{f'_w}{2} \frac{u_{1/3}^2}{g(s-1)d_{50}}, \quad (5)$$

where s is the sediment grain specific gravity (taken here to be 2.65, the value for quartz), g is the acceleration due to gravity, d_{50} is the median grain size, f'_w is the fixed grain wave friction factor computed using Swart’s formula with $2.5d_{50}$ for the physical roughness [Nielsen, 1992], and $u_{1/3}$ is the significant wave orbital velocity (see equation (1)).

[36] The results in Table 2 illustrate several important points: (1) The mean values of the different forcing parameters for each of the bed states are similar for the two frames; (2) the peak wave periods are very similar for the five bed states, differing from 10 s by only ± 10 to 20% on average between bed states; (3) for all bed states and for both frames, the standard deviations of the mean longshore current speed $|V|$, the mean cross-shore current U , the skewness Sk_u and the asymmetry As_u are in every case comparable to or greater than their respective mean values; and (4) in contrast, the standard deviations of u_{rms} are in all cases much smaller than the mean values. Note as well that the standard deviations for the rms infragravity wave velocity are, like those for u_{rms} , comparatively tight. Infragravity velocity increases from the low- to high-energy bed states in Table 2, roughly in proportion to the incident wave velocity, so the two are closely related in these data. However, the mean square infragravity energy is roughly a factor of 25 less than the mean square sea-and-swell energy.

[37] Thus the values in Table 2 indicate, as did the comparisons in Figures 10 and 11, that compared to

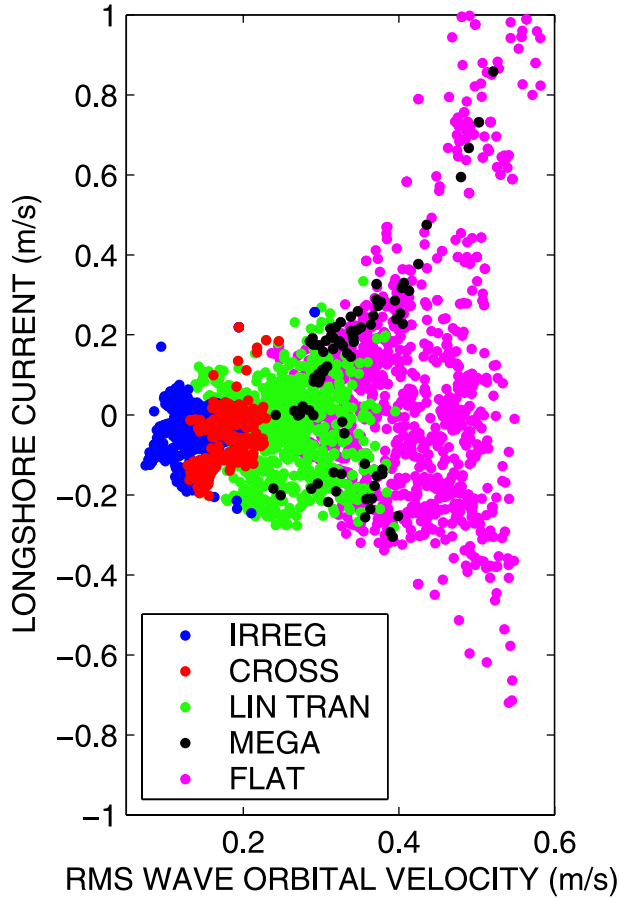


Figure 11. Bed state occurrence as a function of rms wave orbital velocity and longshore current velocity. Colors are as in Figure 10.

u_{rms} , the forcing parameters $|V|$, U , Sk_u and As_u are of little value as predictors of nearshore bed state during SD97.

[38] The number of occurrences N of each bed state are listed in Table 3. Note the relatively low numbers for irregular and cross ripples. These low values result in part from the slower sampling interval during low-energy conditions (30 min compared to 10 min). To correct for this difference, the numbers in the right-hand columns have been adjusted by giving the 30-min sampling intervals a weight of 3 and 10-min intervals a weight of 1. These numbers emphasize the comparative infrequency of lunate megaripples relative to the other bed states. The numbers also emphasize the frequent occurrence of linear transition ripples during SD97.

3.5. Bed State Spectra and Spectral Anisotropy

[39] The distinctive appearance of the different bed states in the fanbeam sonar imagery arises from differences in the range of spatial scales present and their angular distribution. The variations with azimuth of the spatial frequency spectrum for different bedform patterns represent an important aspect of bed state and bottom roughness in sandy environments for which very little quantitative information is available.

[40] Figure 12 shows the azimuthal variation of the seabed backscatter spectrum S_{bb} for irregular, cross, and linear transition ripples, and for flat bed. As indicated in the figure, these spectra are in each case ensemble-averages over several hundred realizations. As expected, the range of scales comprising the spectra, and the azimuthal distribution of these scales, is distinctly different among the four bed states. Flat bed is essentially isotropic, with uniformly low spectral densities (except in the area occupied by the instrument frame). Of the three ripple types, the irregular bed state is the most isotropic. In comparison, the cross-ripple spectrum has a high-energy lobe at low spatial frequencies in the sector between about 220° and 310° (angles positive counterclockwise with respect to the x -axis).

Table 2. Experiment-Mean Hydrodynamic Forcing Parameters Versus Bed State for Frames C and D^a

| | Irregular | Cross | Lin Tran | Mega | Flat |
|-------------------|--------------------|--------------------|--------------------|--------------------|--------------------|
| <i>Frame C</i> | | | | | |
| u_{rms} , m/s | 0.13 ± 0.03 | 0.18 ± 0.03 | 0.25 ± 0.06 | 0.34 ± 0.058 | 0.41 ± 0.08 |
| T_p , s | 11.3 ± 2.6 | 9.7 ± 1.9 | 8.7 ± 2.3 | 8.3 ± 2.4 | 9.5 ± 2.3 |
| $\theta_{2.5}$ | 0.14 ± 0.05 | 0.24 ± 0.06 | 0.43 ± 0.17 | 0.75 ± 0.23 | 1.0 ± 0.35 |
| $ V $, m/s | 0.065 ± 0.067 | 0.051 ± 0.063 | 0.08 ± 0.11 | 0.22 ± 0.21 | 0.25 ± 0.36 |
| U , m/s | -0.038 ± 0.023 | -0.030 ± 0.030 | -0.065 ± 0.046 | -0.071 ± 0.029 | -0.12 ± 0.09 |
| Sk_u | 0.27 ± 0.20 | 0.31 ± 0.15 | 0.23 ± 0.27 | 0.19 ± 0.22 | 0.34 ± 0.25 |
| As_u | 0.008 ± 0.070 | 0.066 ± 0.066 | 0.069 ± 0.064 | 0.059 ± 0.052 | 0.056 ± 0.076 |
| α , deg | -8.8 ± 6.4 | -4.7 ± 5.1 | -1.5 ± 10.3 | 10.6 ± 15.0 | 1.5 ± 13.0 |
| U_{rms}^G , m/s | 0.027 ± 0.006 | 0.034 ± 0.007 | 0.046 ± 0.016 | 0.062 ± 0.020 | 0.099 ± 0.041 |
| <i>Frame D</i> | | | | | |
| u_{rms} , m/s | 0.14 ± 0.02 | 0.18 ± 0.03 | 0.25 ± 0.06 | 0.29 ± 0.08 | 0.43 ± 0.08 |
| T_p , s | 11.5 ± 2.5 | 10.2 ± 2.4 | 9.1 ± 2.2 | 9.2 ± 2.5 | 9.4 ± 2.3 |
| $\theta_{2.5}$ | 0.15 ± 0.05 | 0.23 ± 0.06 | 0.41 ± 0.17 | 0.54 ± 0.26 | 1.1 ± 0.37 |
| $ V $, m/s | 0.047 ± 0.046 | 0.041 ± 0.050 | 0.056 ± 0.072 | 0.09 ± 0.12 | 0.20 ± 0.30 |
| U , m/s | -0.022 ± 0.017 | -0.036 ± 0.021 | -0.038 ± 0.025 | -0.055 ± 0.021 | -0.084 ± 0.051 |
| Sk_u | 0.31 ± 0.90 | 0.31 ± 0.17 | 0.27 ± 0.25 | 0.26 ± 0.20 | 0.32 ± 0.25 |
| As_u | -0.036 ± 0.074 | -0.009 ± 0.060 | 0.004 ± 0.082 | 0.022 ± 0.087 | 0.001 ± 0.081 |
| α , deg | -8.5 ± 4.9 | -4.4 ± 4.3 | -3.7 ± 8.5 | -3.7 ± 10.5 | -0.2 ± 13.9 |
| U_{rms}^G , m/s | 0.027 ± 0.007 | 0.031 ± 0.007 | 0.043 ± 0.015 | 0.050 ± 0.022 | 0.093 ± 0.037 |

^aThe values listed are the means over all instances of each bed state $\pm\sigma$, the standard deviation (except the Shields parameter $\theta_{2.5}$ for which the \pm values are based on the σ for u_{rms}).

Table 3. Number of Occurrences N of Each Bed State, and Corresponding Percent Relative Occurrence for Frames C and D^a

| | C, N | D, N | C, % | D, % | Adjusted C, N' | Adjusted D, N' | Adjusted C, % | Adjusted D, % |
|-----------|-----------|-----------|---------|---------|---------------------|---------------------|------------------|------------------|
| Irregular | 547 | 555 | 6.9 | 7.3 | 1433 | 1423 | 13.5 | 13.8 |
| Cross | 766 | 816 | 9.7 | 10.7 | 1192 | 1276 | 11.2 | 12.3 |
| Lin Tran | 2964 | 3024 | 37.5 | 39.8 | 4082 | 4270 | 38.3 | 41.3 |
| Mega | 636 | 621 | 8.0 | 8.2 | 718 | 631 | 6.7 | 6.1 |
| Flat | 3001 | 2579 | 37.9 | 34.0 | 3224 | 2746 | 30.3 | 26.5 |

^aColumns on the right are adjusted to account for the 10-min sampling interval during storms versus the 30-min interval between storms.

at 0° , as indicated in Figure 12d). The spectral densities in this sector are shifted to higher spatial frequencies for irregular ripples, and the lobe is entirely absent from the linear transition ripple spectrum. The latter spectrum is highly anisotropic, being characterized by two high spectral density lobes on the onshore and offshore sides of the frame centered on spatial frequencies of about 14 m^{-1} , corresponding to a wavelength of 6.7 cm. For comparison, Crawford and Hay [2001] obtained a wavelength of 8.5 cm for this ripple type at the QB95 site.

[41] Figure 13 shows these spectra centered on 180° (offshore), 0° (onshore), and 270° (longshore, northward). The spectra for the flat bed state exhibit low spectral densities which are nearly flat (except at very low spatial frequencies) and nearly identical for the three sectors, i.e., isotropic. In contrast, the spectra for the other bed states are distinctly different both from the flat bed spectrum and from each other. For example, the cross-ripple spectrum for the alongshore sector (Figure 13c) exhibits a pronounced low-frequency peak at 2 cycles/m which either is not present in the spectra for the other bed states or is shifted to higher frequencies (irregular ripples). These results suggest that a spectrum-based anisotropy index could be developed for automatic bed state recognition in rotary sonar imagery.

[42] These results also raise several questions for near-shore sediment dynamics measurement and prediction. What, for example, are the implications with regard to bottom roughness characterization of the pronounced differences in spectral breadth and degree of anisotropy indicated by Figures 12 and 13? In considering this question, one must bear in mind that the rotary fanbeam sonars are more sensitive to differences in bed slope than bed elevation; that is, surfaces sloping toward the transducer produce higher amplitude returns than surfaces which are flat or sloping away. If the one-dimensional bed elevation spectrum at a given azimuth was $\Phi(k, \phi)$, k being the wavenumber ($= 2\pi \times$ the spatial frequency f) and ϕ was the azimuthal angle, and if the fanbeam was a true slope detector, then $\Phi(k, \phi)$ would be proportional S_{bb}/k^2 . The implication is that the low wavenumber components of S_{bb} in Figure 13 likely contribute much more to the overall roughness than the figure indicates. In particular, the low-frequency peaks for irregular and cross ripples in Figure 13c would be amplified relative to their respective high-frequency peaks in Figures 13a and 13b. Predicting these differences in the shape and anisotropy of the small-scale bottom roughness spectrum for different bed states from first principles is a going to be a challenge. On the other hand, for the cross-ripple state especially, parameterizing the roughness with a single

representative height and a single representative wavelength is likely to prove an oversimplification.

3.6. Bed State Scales

[43] Given the discussion in the previous section, it is of interest to determine where the present rippled bed states lie in the canonical two-dimensional parameter space for wave-formed ripples [see Clifton and Dingler [1984, and references therein]. Table 4 summarizes the characteristic wavelengths λ of the irregular, cross, and linear transition ripple states, based on the spectra in Figure 13. A range of scales is given for irregular ripples, while for cross ripples

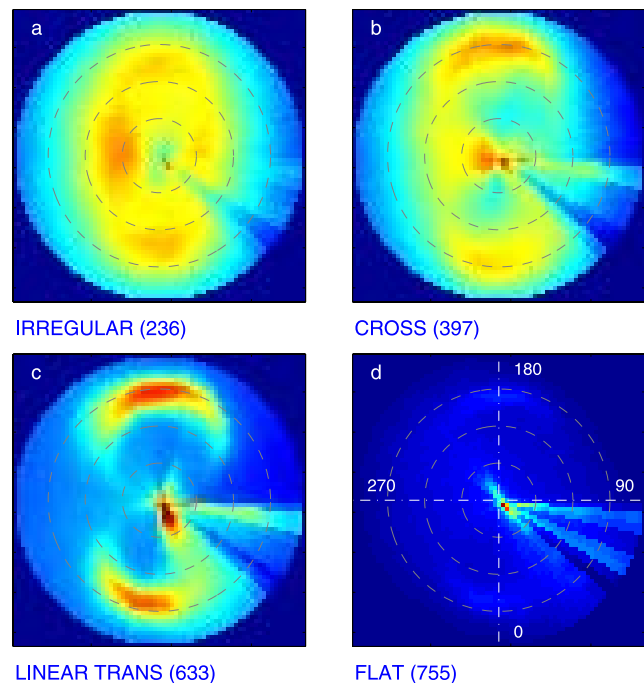


Figure 12. Frame C: Ensemble-averaged radial spectra from the fanbeam images, plotted as a function of azimuthal angle, for (a) irregular ripples, (b) cross ripples, (c) linear transition ripples, and (d) flat bed. Numbers in parentheses indicate the number of spectral images used to compute each ensemble. The color scales are the same for each panel, with red indicating high spectral density, and blue indicating low spectral density. Dashed circles are at 5 cycle/m intervals, increasing outward. The 0° (+x), 90° (+y), 180° , and 270° directions are indicated by the dash-dotted white lines in Figure 12d. Note contamination in the lower right quadrant owing to shadows cast by, and reflections from, the instrument frame.

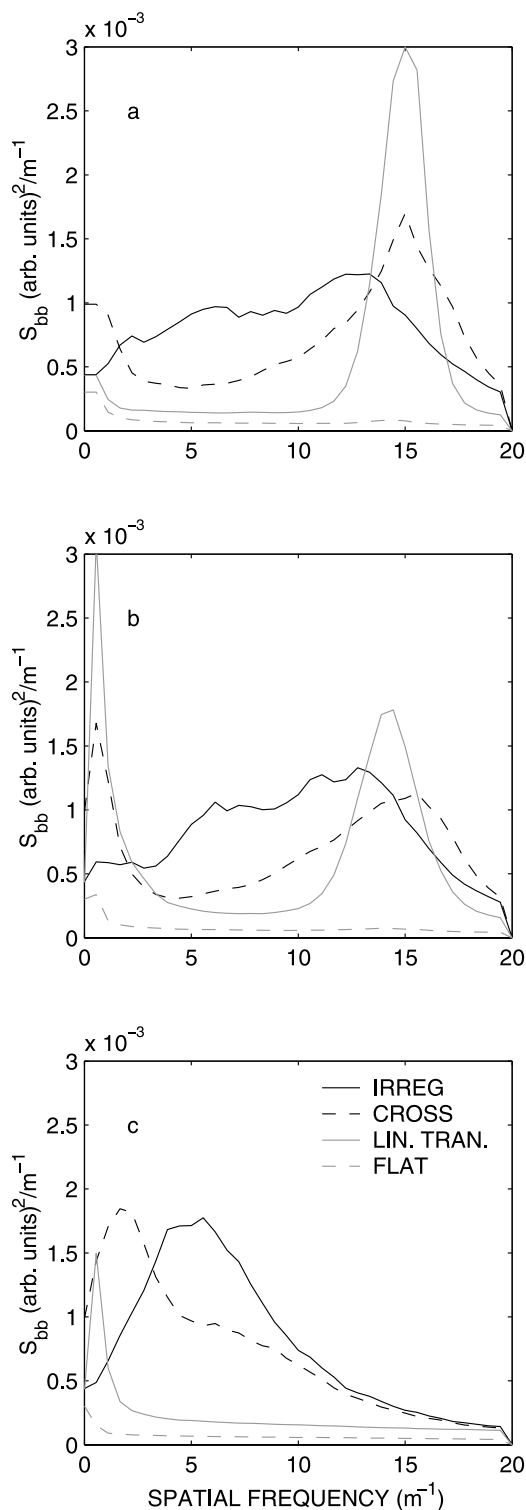


Figure 13. Frame C: Radial spectra from Figure 12 averaged within 4.5° -wide sectors centered on (a) 180° (offshore), (b) 0° (onshore), and (c) 270° (northward).

both a short wavelength scale (from Figure 13a) and a long wavelength scale (from Figure 13c) are listed. Also shown are the corresponding values of the nondimensional parameters λ/d_{50} and $2A/d_{50}$, where A is the significant wave orbital semi-excursion given by $A = u_{1/3}T_p/2\pi$. The linear

transition ripple values are very similar to the QB95 values reported by Crawford and Hay [2001] and, following the Clifton and Dingler [1984] classification scheme, these are anorbital ripples, i.e., $2A \gg \lambda$ and $2A/d_{50} > O(10^3)$. None of the bed states observed at frames C and D satisfy the orbital ripple relationship $\lambda/2A \simeq 0.65-0.8$. All of the $\lambda/2A$ values in Table 4 are substantially lower than 0.65 (by factors of 3 or more), with the exception of the long wavelength cross-ripple component. However, since the crests of this component are oriented obliquely to the angle of wave incidence (Table 2, α), they can hardly be considered to be orbital ripples in the usual sense of the term. The irregular ripples occurred at high values of $2A/d_{50}$ ($>10^3$) and at intermediate values of λ/d_{50} , i.e., above the anorbital value ($\simeq 500$) and below the orbital value ($\simeq 4000$). The irregular ripples are therefore of the suborbital type, and we conclude that true orbital ripples likely did not often occur at frames C and D during SandyDuck97.

3.7. Bed State Storm Cycle

[44] Having demonstrated that the occurrence of different bed states at frames C and D was associated primarily with sea-and-swell wave energy (i.e., the rms wave orbital velocity), we now investigate the temporal evolution of bed state during SD97, and specifically the transition between different states during forcing events. In Figure 14, the co-evolution of rms wave orbital velocity and bed state is shown for the two frame locations.

[45] During the 12 main storm events, there is a clear association between flat bed and high incident wave energy. In contrast, during the periods of relative calm between storms, the bed state time series is dominated by irregular ripples. The other bed states tend to occur at intermediate wave energies during storm growth or decay. Note that flat bed is in some cases also associated with periods of strong longshore currents (Figure 4), but that the longshore current speed need not be high for the bed to be flat.

[46] At both frame locations, the data clearly indicate the repeated occurrence of a bed state cycle associated with each storm event. Typically, the bed state sequence progresses from irregular ripples at the onset of the event, to cross ripples, to linear transition ripples, and then to flat bed at high wave energies. The same sequence occurs during storm wave decay, but in reverse. In some instances, the bed state flipped during the decay phase between flat bed and linear transition ripples as the forcing was modulated by the water depth changes associated with the semi-diurnal tide (e.g., YD266-269, Figure 14b). This occurrence of the same sequence of bed states during periods of increasing and decreasing wave energy, but in reverse order during energy decay, indicates a lack of significant dependence on prior bed state as the bed adjusts to changes in the wave forcing. Specifically, the observations indicate that for the irregular ripple, cross-ripple, linear transition ripple, and flat bed

Table 4. Bed State Scales, Frame C

| Bed State | A , cm | $2A/d_{50}$, ($\times 10^3$) | λ , cm | λ/d_{50} | $\lambda/2A$ |
|---------------------------|-------------|------------------------------------|-------------------|------------------|--------------|
| Irreg | 48 | 6.5 | 7.7–20 | 510–1300 | 0.08–0.21 |
| Cross (short- λ) | 57 | 7.6 | 6.7 | 450 | 0.06 |
| Cross (long- λ) | | | 50 | 3300 | 0.44 |
| Lin Tran | 69 | 9.3 | 6.7 | 450 | 0.05 |

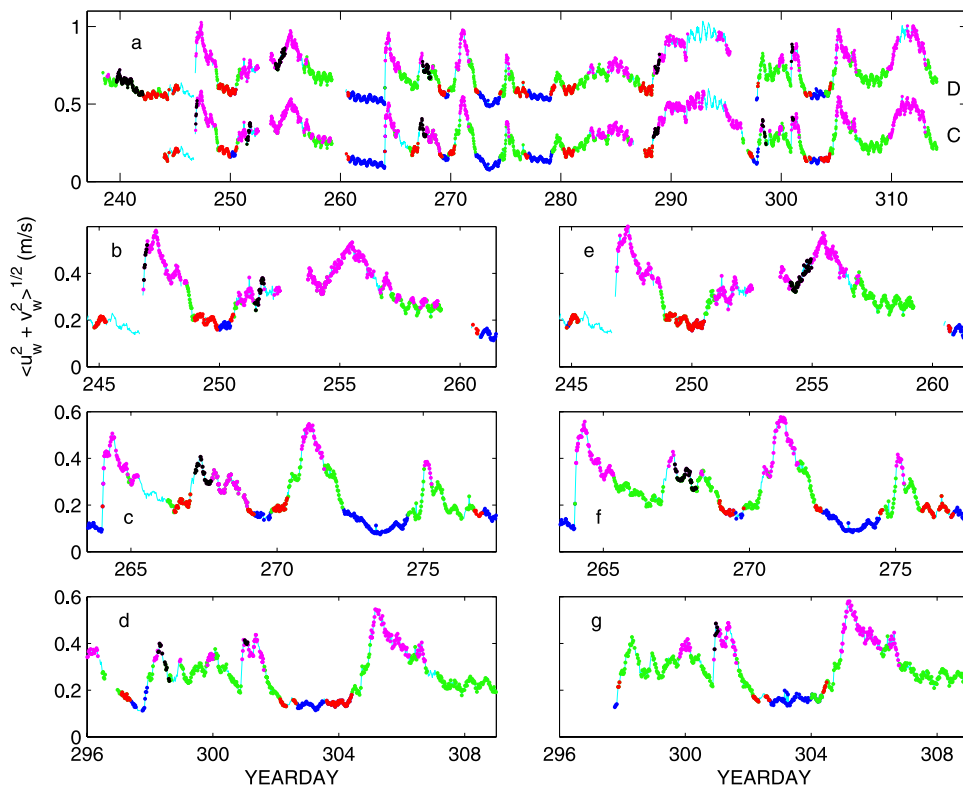


Figure 14. Bed state storm cycle, frames C and D: (a) complete record (with a 0.4 m/s offset applied to the frame D data), (b, c, d) expanded views of selected time segments at frame C, and (e, f, g) the same segments at frame D. Bed states are indicated by colored dots, as in Figures 10 and 11: irregular ripples (blue), cross ripples (red), linear transition ripples (green), lunate megaripples (black), and flat bed (magenta). During the 7 days prior to YD244 at Frame C, the dominant bed states (not shown) were lunate megaripples and linear transition ripples.

states, and for the $O(1)$ -hour to $O(100)$ -hour timescales associated with tidal and weather-dependent changes in wave energy, bed state adjustment did not strongly depend on prior bed state.

[47] Lunate megaripples occurred infrequently and at different times at these two locations, i.e., at frame D either later by as much several days, or not at all (compare Figures 14b and 14e, 14c and 14f, and 14d and 14g). Cross ripples sometimes did not occur: for example, Figure 14c, YD274. The distinction between cross-ripple and irregular ripple states was the source of most of the discrepancies between observers because the two states often co-exist in the sonar image. Thus it is possible and even probable that the occasional non-occurrence of cross ripples is partly due to the unavoidable subjectivity of visual bed state identification. It is also possible, however, that the conditions for cross-ripple formation involve more than the rms wave orbital velocity, as is clearly the case for lunate megaripples.

4. Discussion

4.1. Comparison to Clifton's Conceptual Model

[48] There are four governing parameters in Clifton's [1976] model: (1) the maximum wave orbital velocity u_m during a wave half-cycle, (2) the velocity amplitude difference Δu_m between the shoreward and seaward strokes of the wave, (3) the sediment median grain diameter d_{50} , and (4) the wave period T .

[49] The parameter Δu_m , called asymmetry by Clifton [1976], is related to but different from the asymmetry discussed here. As pointed out elsewhere [e.g., Elgar and Guza, 1985], there are two "asymmetries" to consider in a time series: asymmetry about the horizontal axis (i.e., Sk , equation (2)), and asymmetry about the vertical axis (i.e., As , equation (3)). Clifton's Δu_m parameter is related primarily to Sk since, for a pure sawtooth wave (zero Sk , nonzero As), Δu_m is identically zero.

[50] In purely physical terms, the question of interest here is whether wave nonlinearity plays a significant role in bed state occurrence, compared to wave energy alone. Sk_u and As_u are energy-normalized measures of wave nonlinearity, and as such enable the effects of wave energy and wave nonlinearity on bed state to be investigated separately. This is not the case for the parameter Δu_m which, for a given skewness, would vary with wave energy. These points are illustrated as follows. Let

$$u = u_o \left[\cos \omega t + \sum_{n=2}^M \epsilon^{n-1} \cos n\omega t \right] \quad (6)$$

represent a nonlinear wave. The first term is the fundamental, with angular frequency ω . The additional terms are harmonics phase-locked to the fundamental, but with amplitudes reduced by increasing powers of the (small) parameter ϵ . With $M = 4$, equation (6) produces skewed waveforms (Figure 15) which are well behaved for $0 < \epsilon <$

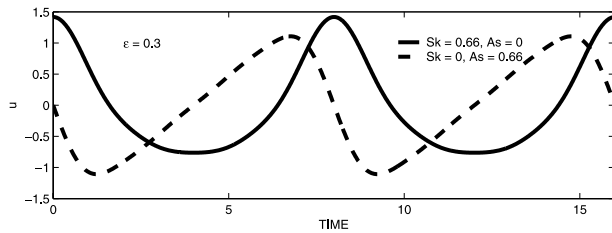


Figure 15. Skewed and asymmetric waveforms from equation (6) with $M = 4$ and $\epsilon = 0.3$. For the asymmetric forms, the cosines in equation (6) were replaced with sines.

0.4. (By well behaved we mean that waves with periods shorter than that of the dominant waveform are not apparent.) For this range of ϵ , the resulting skewnesses range from 0 to 0.9, comparable to the range of observed values (Figures 5 and 6). Further, the skewnesses over this range of ϵ are largely determined by the first harmonic (to within better than 10%), given analytically by $Sk = 3\epsilon/\sqrt{2}$. Thus skewnesses obtained from equation (6) are independent of u_o , and therefore of the wave energy, $u_o^2/2$ (neglecting terms of $O(\epsilon^2)$ or smaller). In contrast, Clifton's [1976] Δu_m is given by the difference between the peak speed $u_{m+} \simeq u_o(1 + \epsilon)$ under the crest and that under the trough $u_{m-} \simeq u_o(1 - \epsilon)$, again dropping terms of $O(\epsilon^2)$ or less. Thus $\Delta u_m \simeq 2u_o\epsilon$, which contains the skewness, but also depends explicitly on wave energy. The same argument can be extended to asymmetry, as an asymmetric waveform is obtained from equation (6) by replacing cosines with sines (Figure 15). The asymmetry is then obtained from the imaginary part of the Hilbert transform (equation (3)), which is equivalent to phase-shifting each term by $\pi/2$, i.e., giving equation (6) again. Thus the normalized third moments, Sk and As , are amplitude-independent measures of the departure from the sinusoidal wave shape predicted by linear theory, and are therefore the appropriate measures of wave nonlinearity in the present context.

[51] While the argument above is concerned only with local wave shape, and not with the nonlinear dynamics giving rise to wave shape, it is relevant nevertheless to place the present observations in the general context of nonlinear wave theory. First, making use of the experimental result that linear theory can be applied locally [Guza and Thornton, 1980] and taking the typical peak wave period T_p to be 10 s (Table 2), the linear dispersion relation for surface gravity waves ($\omega^2 = gk \tanh kh$, k the wavenumber, h the water depth) gives $k = 0.118 \text{ m}^{-1}$ for 3 m depth. For comparison, the shallow water result ($k = \omega/\sqrt{gh}$) is 0.116 m^{-1} ; thus waves with period $T_p \simeq 10$ s are nearly shallow-water here, and weakly dispersive. In the Stokes expansion for weakly nonlinear waves in constant depth [e.g., Wiegand, 1960; Mei, 1989], the expansion parameter is the Ursell number $U_r = k\eta_o/(kh)^2$, where η_o is the surface elevation amplitude. With $\eta_o = u_o/\omega$, and u_o equal to $u_{1/3} = 2u_{rms}$, the values of u_{rms} in Table 2 give $0.03 \leq U_r \leq 0.8$. The Stokes expansion is expected to apply only for $U_r < 0.3$ [Guza and Thornton, 1980], which corresponds to less than half the observed range of values (and, since T_p is nearly constant, to lower wave energies). Nonetheless, the Stokes expansion is clearly relevant, and the coefficient of the first harmonic in the expansion, corresponding to ϵ in

equation (6), is $3U_r/4 = 3ku_o/[4\omega(kh)^2]$. On the basis of this relation, skewness should increase with increasing wave energy, at least in the low-energy range. However, neither the values in Table 2 nor the scatter plots in Figure 10 indicate such a trend in the experiment-mean sense.

[52] This absence in the observations of a relationship between rms wave orbital velocity and wave skewness (or asymmetry) is indicative of the complexity of the nonlinear interactions among the spectral constituents of the shoaling wave field. The values of asymmetry and skewness at a given location on the beach profile which result from these interactions have been shown to depend on the directional as well as the frequency distribution of incident sea-and-swell wave energy [Herbers and Burton, 1997]. Thus, since these distributions will necessarily differ from storm to storm, and since the beach profile itself evolved with time over the 75-day duration of the experiment, the observed wide range of skewness and asymmetry values for a given incident wave energy is to be expected. Furthermore, for a given locally observed energy in the incident sea-and-swell band, skewness and asymmetry depend on both sum and difference interactions among the spectral constituents [Hasselmann et al., 1963]. The difference interactions can be important in the sediment dynamics context, since negative skewnesses arising from difference interactions in a bimodal sea-and-swell spectrum have been found to be well correlated with offshore ripple migration [Crawford and Hay, 2001, 2003]. In contrast, the Stokes expansion admits only sum interactions (i.e., higher-frequency harmonics of the fundamental), and the predicted skewnesses are positive definite. Thus the Stokes expansion and other nonlinear theories for regular (i.e., periodic) waves, such as cnoidal theory, cannot reproduce the range of skewnesses and asymmetries encountered in field conditions.

[53] The preceding discussion underscores the importance of long time series of bed evolution measurements for identifying the relative importance of wave energy and wave nonlinearity in relation to bed state occurrence, and the results presented in section 3 can now be used as a basis against which to test the concepts proposed by Clifton [1976]. The Frame C and D data from SD97 are particularly well suited to an investigation of the importance of third-moment statistics in bed state prediction because (1) the grain size distribution parameters at the two frames are nearly identical (Table 1), thus effectively eliminating the parameter d as a contributor to the observed bed state variability at these two locations; (2) the peak wave period T_p (Table 2) is nearly identical for the five bed states considered, with the possible exception of the irregular ripple state (discussed further below), thus eliminating the parameter T ; and (3) the experiment-mean values of u_{rms} and the related parameter $\theta_{2.5}$ are, with the possible exception of lunate megaripples, nearly identical at the two frames for a given bed state. (For the irregular waves typical of field conditions, some representative wave is needed; following common practice, we use the significant wave orbital velocity $u_{1/3} = 2u_{rms}$ for the amplitude, and T_p for the period. Note that in equation (6) the wave amplitude is nearly independent of ϵ since, by definition, the amplitude is given by half the peak-to-trough velocity difference, i.e., amplitude = $(u_{m+} + u_{m-})/2 = u_o + O(\epsilon^2)$. Thus $u_{1/3}$ or

equally u_{rms} with the factor of 2 understood is our equivalent of Clifton's u_m .)

[54] The ± 2 -s standard deviations for the values of T_p in Table 2 indicate significant overlap in the range of wave periods for which the different bed states occurred. The consistently longer experiment-mean wave periods for irregular ripples, 11 s compared to 9 s for the other bed states (Table 2), can be understood physically. Irregular ripples tended to occur at low wave energies between storms when the incident wave field was dominated by smaller-amplitude, longer-period swell from distant sources. Thus the 20% longer wave periods on average for irregular ripples is probably a matter of circumstance, as opposed to one of causation. Consequently, we do not consider peak wave period to have been an important determining factor in the development of any of the five bed states, at least not in the experiment-mean sense.

[55] Thus, with grain size and wave period eliminated, and given the results and discussion in section 3.4, there seems to be no basis within the context of the SD97 data presented here for including wave nonlinearity in predictive models of bed state occurrence in the nearshore zone, at least not for the range of skewness and asymmetry values encompassed by these data (and with the possible exception of lunate megaripples, see below). Consequently, we conclude that among u_{rms} , Sk_u and As_u the critical parameter for bed state occurrence during SD97 was u_{rms} . This conclusion would lead to the prediction, in reference to equation (6), that the same bed state would occur for waves with zero or nonzero skewness, but the same energy (to $O(\epsilon^2)$). Thus our results indicate that the differences in transport over a wave cycle arising from skewness and/or asymmetry were not of first-order importance for bed state occurrence during SD97. If this result were to hold generally, then the incorporation of bed state in sediment dynamics and wave dissipation models for sandy seabed environments could be greatly simplified.

4.2. Lunate Megaripples

[56] During the experiment the transitions to irregular ripples, linear transition ripples, cross ripples, and flat bed could all be anticipated as storm waves grew or decayed; that is, these bed states were usually part of the bed state storm cycle. In contrast, lunate megaripples did not appear consistently or predictably, or at all for many of the storm events (Figure 14). Thus wave forcing energy alone does not appear to have been a sufficient condition for lunate megaripple occurrence during SandyDuck97, unless these features actually did occur regularly but sometimes outside the field of view of the rotary sonars. The latter possibility notwithstanding, the occurrence conditions for lunate megaripples are not properly represented by the single experiment-mean values in Table 2. Once these bedforms became large (i.e., several meters in horizontal extent like the feature in Figure 7), they could persist for a day or longer, during which time the wave forcing conditions changed substantially (e.g., Figure 14a, frame D, YD 240+). Consequently, these meter-scale bedforms, like the meter-scale orbital ripples investigated by *Traykovski et al.* [1999], are likely to exhibit significant hysteresis in their temporal histories. This hysteresis, and the small number of realizations relative to the other bed states discussed here, are likely to have

resulted in $\theta_{2.5}$ values for lunate megaripples with a wider range than that corresponding to their initial genesis, and to have contributed to the apparent difference in the experiment-mean values of $\theta_{2.5}$ between frames C and D.

4.3. Ripple Asymmetry

[57] In his conceptual model, *Clifton* [1976] also discusses the effects of wave nonlinearity on ripple asymmetry, referring in this case to asymmetry in the same sense as that used here, that is, with respect to the vertical axis [see *Clifton*, 1976, Figure 6]. The backscatter spectra in Figures 13a and 13b for linear transition ripples exhibit a higher peak spectral density on the seaward side of the frame than on the shoreward side. This difference in peak spectral density indicates that the shoreward facing slopes of these ripples were steeper than the seaward facing slopes. Together with the fact that wave orbital velocity skewnesses were predominantly positive during SD97 at frame C, steeper shoreward facing slopes indicate shoreward migration. This interpretation is consistent with the observed relationship between measured ripple asymmetry and wave orbital velocity skewness for linear transition ripples during QB95 [*Crawford and Hay*, 2001]. Shoreward facing lunate megaripples are asymmetric, being pitched forward in the shoreward direction, which was also their dominant migration direction during Duck94 [*Ngusaru and Hay*, 2004]. The lunate megaripples observed during SD97 also migrated primarily shoreward. The fanbeam spectra for cross ripples exhibit onshore-offshore asymmetry at high wavenumbers similar to the linear transition ripple spectra, again suggesting shoreward migration, which is again consistent with the positive values of Sk_u for this bed state (Table 2). Movies made of the fanbeam images clearly indicate shoreward migration during the times that cross ripples were present. In contrast, the irregular ripple spectra are quite symmetric despite the experiment-mean value of Sk_u being similar to those for the other bed states. The experiment-mean Shields parameter for irregular ripples was only 0.1, however, which is only a factor of 2 above the threshold for grain movement (0.05 [it *Nielsen*, 1992]). Thus the weaker asymmetry of these ripples likely corresponds to the less active conditions when they were present, and to the offsetting effects on ripple migration of positive wave orbital velocity skewness and offshore mean currents (Table 2).

5. Summary and Conclusions

[58] Results have been presented from 70+ days of rotary acoustic images of the seabed during SandyDuck97 at two locations in 3.4-m and 3.3-m mean water depths separated by 40-m cross-shore distance. The images indicate the occurrence of five principal bed states: irregular ripples, cross ripples, linear transition ripples, lunate megaripples, and flat bed. Of these bed states, linear transition ripples and flat bed were the most frequent, respectively occurring in 39% and 36% of the images, and approximately 40% and 28% of the time that these five bed states were present.

[59] Intercomparisons between second- and third-order forcing statistics from independent sensors on the same instrument frame, and from instruments at different cross-shore locations, yield acceptable overall agreement. Second-

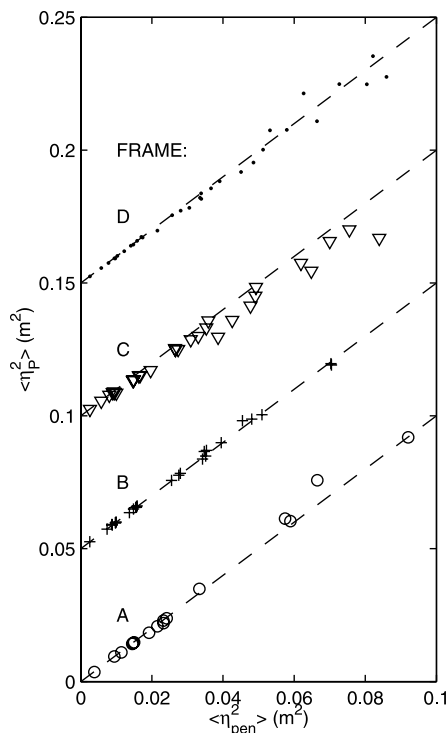


Figure A1. Pressure versus upward looking sonar sea surface elevation variance comparison: frame A (\circ), frame B (+), frame C (\triangle), and frame D (\cdot). R^2 is as follows: A, 0.993; B, 0.998; C, 0.985; and D, 0.986. Best-fit slopes $m \pm 95\%$ bootstrap confidence intervals are as follows: A, 1.04 ± 0.025 ; B, 1.04 ± 0.008 ; C, 0.89 ± 0.018 ; and D, 0.98 ± 0.019 .

order statistics are in reasonable agreement with the predictions of linear wave theory.

[60] The relative importance of third-order (skewness and asymmetry) and second-order (wave energy, represented by rms velocity) wave statistics to the occurrence of different bed states is investigated in the context of Clifton's [1976] conceptual model of nearshore bed state development. In this model, bed state depends on four parameters: wave energy, wave skewness, wave period, and sediment grain size. The conditions at these two locations (very similar sediment grain size distributions, very similar experiment-mean wave periods across bed states) enabled us to eliminate wave period and grain size as independent variables and focus on the effects of wave energy, skewness, and asymmetry. We find that the occurrence of four of the five bed states (lunate megaripples are a possible exception) during SandyDuck97 depended primarily upon rms wave orbital velocity, and that third-order moments did not play a discernible role in the occurrence of these four bed states at the two locations.

[61] Radial spectra of the irregular ripple, cross-ripple, linear transition ripple, and flat bed states indicate pronounced differences in isotropy as a function of spatial scale. For the rippled beds, the irregular ripples were the most isotropic, and linear transition ripples were the least. For the cross-ripple and linear transition ripple states, factor of 2 differences in peak spectral levels between the onshore and offshore directions were observed, with higher back-

scatter energies on the seaward side of the frame. These two ripple types usually migrated shoreward during the deployment and, since ripple asymmetry is often associated with ripple migration and net bedload transport, it is very likely that the onshore-offshore differences in backscatter spectral densities reflect differences in ripple asymmetry due to shoreward migration and shoreward net bedload transport. Since net transport in waves is related to the third-order velocity moments, and the wave skewnesses were mainly positive during the experiment, the onshore-offshore asymmetry of the ripple profiles implied by the radial backscatter amplitude spectra is expected. Thus, although the results from this experiment indicate that bed state occurrence was largely independent of the third-order moments of the wave field (counter to the predictions of Clifton's [1976] conceptual model), the third-order moments do appear to play a significant role in determining ripple profile asymmetry, consistent with one of the predictions of Clifton's model.

[62] Lunate megaripples represent a special case. Like the other bed states, lunate megaripples occurred within a well-defined band of wave energies. Unlike the other bed states, however, these bedform types did not appear repeatedly during the course of the experiment. We suggest that lunate megaripple occurrence may depend on some additional factor, that is, a factor different from incident wave energy alone. Individual lunate megaripples have the further special property, once grown to 1-m and larger horizontal scales, of persisting for $O(1)$ day through a range of forcing conditions. The large physical size of these features therefore indicates a longer response time and the likelihood that they evolve out of equilibrium with the forcing.

[63] The bed state time histories (again, excepting lunate megaripples) at the two locations clearly and repeatedly indicate the existence of a bed state storm cycle. Through the course of more than 10 separate storm events, this cycle manifested itself as a temporal progression during storm wave growth from an initial irregular ripple state through cross ripples to linear transition ripples and then to flat bed, followed by the reverse sequence during wave decay. The occurrence of the same sequence of bed states during both storm wave growth and decay, but in reverse order during decay, indicates a lack of dependence on prior bed state over the $O(1)$ -hour to $O(100)$ -hour timescales associated with tidal and storm-induced changes in wave energy. Within the cycle, each of the different bed states occurred repeatedly within a relatively narrow and distinct range of incident wave energies. This high degree of repeatability, the apparent lack of significant dependence on prior bed state, and the primary dependence on wave energy rather than wave nonlinearity all substantially reduce the conceptual difficulties associated with incorporating bed state in predictive models of fluid/sediment dynamics in sandy nearshore environments.

Appendix A

[64] Surface elevation measurements were made using 2.25-MHz pencil-beam sonars (like the rotary fanbeams, also Model 971), operated in upward looking mode. These runs were not part of the routine data collection protocol, but were carried out intermittently on an opportunistic basis

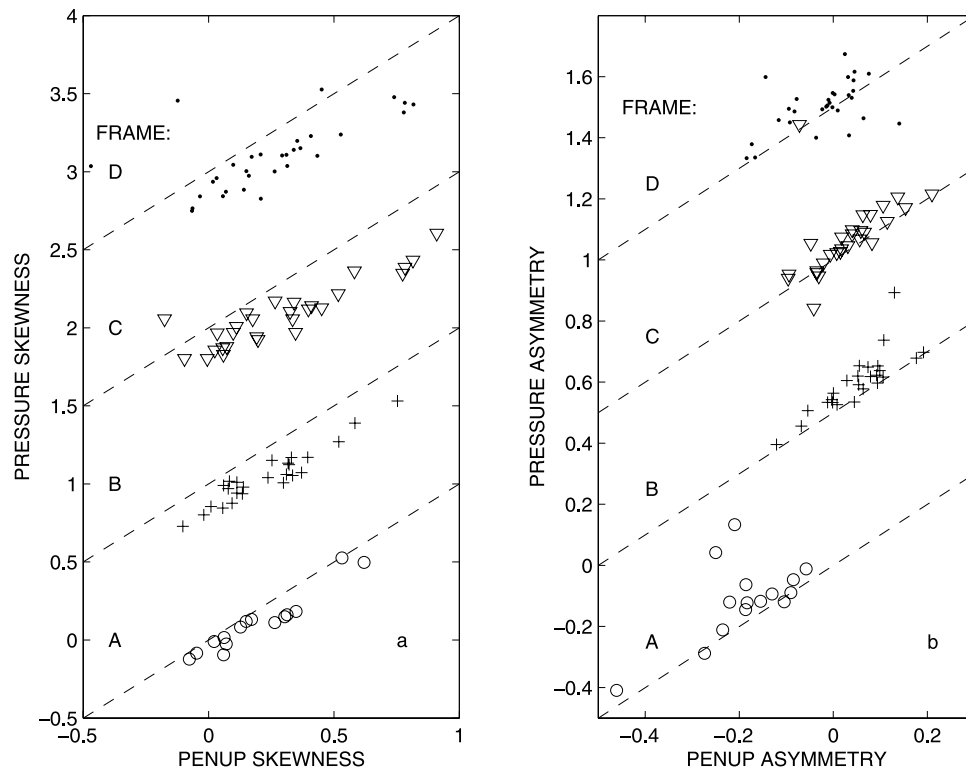


Figure A2. Pressure versus upward looking sonar sea surface elevation skewness-asymmetry comparison. Symbols are as in Figure A1. Skewness R^2 is as follows: A, 0.993; B, 0.998; C, 0.985; and D, 0.986. Skewness best-fit slopes $m \pm 95\%$ bootstrap confidence intervals are as follows: A, 1.04 ± 0.025 ; B, 1.04 ± 0.008 ; C, 0.89 ± 0.018 ; and D, 0.98 ± 0.019 . Asymmetry R^2 is as follows: A, 0.993; B, 0.998; C, 0.985; and D, 0.986. Asymmetry best-fit slopes $m \pm 95\%$ bootstrap confidence intervals are as follows: A, 1.04 ± 0.025 ; B, 1.04 ± 0.008 ; C, 0.89 ± 0.018 ; and D, 0.98 ± 0.019 .

through the course of the experiment. During conditions of active wave breaking, the bubble injection events associated with local breakers, and the bubble clouds advected into the frame area from breaking events elsewhere, masked the surface echo intermittently. Thus the data presented here are from selected runs and run segments for which breaking events were either absent or very infrequent. Surface elevation variance was determined from the pressure sensor using the linear surface gravity wave dispersion relation for arbitrary water depth to migrate the spectral densities at depth to the sea surface. Surface elevation variances from the pressure sensors and the upward looking sonars on each instrument frame are presented in Figure A1. Pressure skewness and asymmetry were computed from the time series converted to elevation assuming hydrostatic pressure. Surface elevation skewness and asymmetry are compared in Figure A2.

[65] **Acknowledgments.** The authors thank the personnel at the FRF and W. Birkemeier in particular for their hospitality and support during SandyDuck97. We also thank C. Smyth and R. Speller for carrying out the tedious visual classification of the sonar images, Wes Paul and Robert Craig for their invaluable development and maintenance of the hardware and software components of the rotary sonar data acquisition and control system, Tony Bowen for providing us with the EM flowmeter and pressure sensor data, and Steve Henderson for carrying out the initial quality control of those data, and we acknowledge the able assistance of the other members of the field team. We also thank Bob Guza for directing us to the asymmetry results of *Herbers et al.* [2003]. This research was supported by grants from the Collaborative Special Projects program of the Natural Sciences and

Engineering Council of Canada, and from the Coastal Sciences program of the U.S. Office of Naval Research.

References

- Birkemeier, W. A., H. C. Miller, S. D. Wilhelm, A. E. DeWall, and C. S. Gorbics (1985), A User's guide to the Coastal Engineering Center's (CERC's) Field Research Facility, *Tech. Rep. CERC-85-1*, 137 pp., Coastal Eng. Res. Cent., U.S. Army Corps of Eng., Washington, D. C.
- Clifton, H. E. (1976), Wave-formed sedimentary structures—A conceptual model, in *Beach and Nearshore Sedimentation, Spec. Publ. 24*, edited by R. A. Davis Jr. and R. L. Ethington, pp. 126–148, Soc. for Sed. Geol. (SEPM), Tulsa, Okla.
- Clifton, H. E., and J. R. Dingler (1984), Wave-formed structures and paleoenvironmental reconstruction, *Mar. Geol.*, *60*, 165–198.
- Clifton, H. E., R. E. Hunter, and R. L. Phillips (1971), Depositional structures and processes in the non-barred high-energy nearshore, *J. Sediment. Petrol.*, *41*(3), 651–670.
- Conley, D. C., and D. L. Inman (1992), Field observations of the fluid-granular boundary layer under near-breaking waves, *J. Geophys. Res.*, *97*(C6), 9631–9643.
- Crawford, A. M., and A. E. Hay (2001), Linear transition ripple migration and wave orbital velocity skewness: Observations, *J. Geophys. Res.*, *106*(C7), 14,113–14,128.
- Crawford, A. M., and A. E. Hay (2003), Wave orbital velocity skewness and linear transition ripple migration: Comparison with weakly nonlinear theory, *J. Geophys. Res.*, *108*(C3), 3091, doi:10.1029/2001JC001254.
- Dingler, J. R., and D. L. Inman (1977), Wave-formed ripples in nearshore sands, paper presented at 15th Coastal Engineering Conference, Am. Soc. of Civ. Eng., New York.
- Elgar, S. (1987), Relationships involving third moments and bispectra of a harmonic process, *IEEE Trans. Acoust. Speech Signal Process.*, *ASSP-35*(12), 1725–1726.
- Elgar, S., and R. T. Guza (1985), Observations of bispectra of shoaling surface gravity waves, *J. Fluid Mech.*, *161*, 425–448.

- Elgar, S., M. H. Freilich, and R. T. Guza (1990), Model-data comparisons of moments of nonbreaking shoaling surface gravity waves, *J. Geophys. Res.*, *95*(C9), 16,055–16,063.
- Fofonoff, N. (1969), Spectral characteristics of internal waves in the ocean, *Deep Sea Res.*, Suppl., *16*, 58–71.
- Gallagher, E. L., S. Elgar, and E. D. Thornton (1998), Observations and predictions of megaripple migration in a natural surf-zone, *Nature*, *394*(6689), 165–168.
- Guza, R. T., and E. B. Thornton (1980), Local and shoaled comparisons of sea surface elevations, pressures and velocities, *J. Geophys. Res.*, *85*(C3), 1524–1530.
- Hasselmann, K., W. Munk, and G. MacDonald (1963), Bispectra of ocean waves, in *Time Series Analysis*, pp. 125–139, John Wiley, Hoboken, N. J.
- Hay, A. E., and A. J. Bowen (1993), Spatially correlated depth changes in the nearshore zone during autumn storms, *J. Geophys. Res.*, *98*(C7), 12,387–12,404.
- Hay, A. E., and D. L. Wilson (1994), Rotary sidescan images of nearshore bedform evolution during a storm, *Mar. Geol.*, *119*, 57–65.
- Henderson, S. M., and A. J. Bowen (2002), Observations of surf beat forcing and dissipation, *J. Geophys. Res.*, *107*(C11), 3193, doi:10.1029/2000JC000498.
- Herbers, T. H. C., and M. C. Burton (1997), Nonlinear shoaling of directionally spread waves on a beach, *J. Geophys. Res.*, *102*(C9), 21,101–21,114.
- Herbers, T. H. C., M. Orzech, S. Elgar, and R. T. Guza (2003), Shoaling transformation of wave frequency-directional spectra, *J. Geophys. Res.*, *108*(C1), 3013, doi:10.1029/2001JC001304.
- Kundu, P. K. (1990), *Fluid Mechanics*, 638 pp., Elsevier, New York.
- Mei, C. C. (1989), *The Applied Dynamics of Ocean Surface Waves*, *Adv. Ser. Ocean Eng.*, vol. 1, 740 pp., World Sci., Hackensack, N. J.
- Ngusaru, A. S., and A. E. Hay (2004), Cross-shore migration of lunate megaripples during Duck94, *J. Geophys. Res.*, *109*, C02006, doi:10.1029/2002JC001532.
- Nielsen, P. (1992), *Coastal Bottom Boundary Layers and Sediment Transport*, 324 pp., World Sci., Hackensack, N. J.
- Sleath, J. F. A. (1984), *Sea Bed Mechanics*, 335 pp., John Wiley, Hoboken, N. J.
- Smyth, C., A. E. Hay, and L. Zedel (2002), Coherent Doppler Profiler measurements of near-bed suspended sediment fluxes and the influence of bedforms, *J. Geophys. Res.*, *107*(C8), 3105, doi:10.1029/2000JC000760.
- Thornton, E. B., and R. T. Guza (1983), Transformation of wave height distribution, *J. Geophys. Res.*, *88*(C10), 5925–5938.
- Traykovski, P., A. E. Hay, J. D. Irish, and J. F. Lynch (1999), Geometry, migration, and evolution of wave orbital ripples at LEO-15, *J. Geophys. Res.*, *104*(C1), 1505–1524.
- Wiegel, R. L. (1960), *Oceanographical Engineering*, 532 pp., Prentice-Hall, Upper Saddle River, N. J.

A. E. Hay and T. Mudge, Department of Oceanography, Dalhousie University, Halifax, NS, Canada, B3H 4J1. (alex.hay@phys.ocean.dal.ca)